



# Lift Equivalence and Cancellation for Airfoil Surge–Pitch–Plunge Oscillations

Kelsey H. Elfering\* and Kenneth O. Granlund†  
North Carolina State University, Raleigh, North Carolina 27695

<https://doi.org/10.2514/1.J059068>

A NACA 0018 airfoil in freestream velocity is oscillated in longitudinal, transverse, and angle-of-attack directions with respect to the freestream velocity, known as surge, plunge, and pitch. The lift-based equivalence method introduces phase shifts between these three motions to construct in-phase sinusoidal components for maximum lift, waveform construction. Lift cancellation is also determined with the exact negative pitch and plunge motion amplitudes found from the equivalence method to achieve out-of-phase wave destruction. Lift cancellation occurs when a combination of these motions is sought to obtain a constant lift magnitude throughout the oscillation cycle. To achieve both equivalence and cancellation of lift, a prescribed pure pitch amplitude through the Theodorsen theory equates the corresponding equivalent plunge amplitude and pitch–plunge phase shift. These Theodorsen, linear superposition findings of pitch–plunge are leveraged toward the Greenberg theory to determine a closed-form, surge–pitch–plunge solution through the addition of a surge–plunge phase shift and optimal surge amplitude for lift cancellation. The lift cancellation surge–pitch–plunge amplitudes define the equivalence amplitude investigated here and theoretically limit the experiment to combinations of the first lift harmonic of the Greenberg theory. The analytical results are then compared with experimental lift force measurements and dye visualization. The normalized lift differences due to unsteady wake and boundary-layer behavior are examined to explore the extents of the Greenberg theory for these cases of lift-based equivalence and cancellation.

## Nomenclature

$a$	=	pitch, pivot point
$b$	=	one-half of the chord length, m
$C(k)$	=	Theodorsen's function
$C_l$	=	airfoil lift coefficient
$c$	=	airfoil chord, m
$F(k)$	=	real part of the Theodorsen function
$f$	=	physical frequency, 1/s
$G(k)$	=	imaginary part of the Theodorsen function
$h$	=	plunge displacement, m
$k$	=	reduced frequency, $\omega c / (2v_0)$
$L$	=	airfoil lift, N
$Re$	=	Reynolds number based on airfoil chord ( $\rho v_0 c / \mu$ )
$T$	=	time period, s
$t$	=	time, s
$v_0$	=	freestream velocity, m/s
$X$	=	surge, longitudinal displacement, downstream positive, m
$x_p$	=	chordwise distance from the leading edge to the pivot point, m
$\alpha$	=	angle of attack, deg
$\theta$	=	pitch angle displacement, deg
$\mu$	=	dynamic viscosity of water ( $10^{-3}$ Pa · s)
$\rho$	=	density of water ( $1000$ kg/m <sup>3</sup> )
$\sigma$	=	surge amplitude with respect to freestream velocity
$\phi$	=	phase shift for plunge from surge, deg
$\Psi$	=	phase shift for pitch from plunge, deg
$\omega$	=	circular frequency ( $2\pi f$ ), deg / s

## Subscripts

$g$	=	Greenberg's approach
$m$	=	maximum displacement (amplitude)
$qs$	=	quasi-steady thin-airfoil-theory approach
$t$	=	Theodorsen's approach

## I. Introduction

UNSTEADY aerodynamics includes flow conditions that are not fully understood or confidently predicted for low reduced frequency, shed vortical structures, large motion amplitudes, and other time-varying aerodynamics. Conditions on airfoils experiencing unsteady aerodynamics have been broadly studied, predominantly for helicopters in hovering and forward flight. Similar flow phenomenon also occurs in wind turbines, flapping wing, slowed rotors, and many unmanned aerial vehicle configurations. Understanding the aerodynamics and kinematics of these types of flow–motion interactions can improve functionality toward the intended aeromechanics purposes, and improve optimization routines from closed-form solutions.

Of interest is the investigation of analytical lift-based equivalence and cancellation for airfoils undergoing surge–pitch–plunge combinations. The cross section of an airfoil can undergo vertical displacement, rotation, and streamwise displacement with respect to the freestream fluid flow: referred to as plunge, pitch, and surge. To better understand the underlying flow physics, the experiments conducted intend to combine these individual dynamic motions that largely influence unsteady aerodynamics.

Lift-based equivalence occurs when the individual lift contributions of surge, pitch, or plunge are near-constant amplitude compared with each other despite undergoing dynamic motions. Lift-based cancellation is the combination of these individual components to achieve a static lift amplitude, despite undergoing large, pulsating motions that would typically create large deviations in lift compared with that of an airfoil at constant incidence and freestream flow velocity. Including surge as part of this investigation expands on past works that have examined only linear superposition of pitch and plunge.

These predominantly rotor-type applications have complex flow-fields, often with multiple blades rotating through compressible flow. Frequently, complicated unsteady research is reduced to cases of

Presented as Paper 2019-3337 at the 2019 AIAA Aviation Forum, Dallas, TX, January 17–21, 2019; received 18 September 2019; revision received 6 April 2020; accepted for publication 22 May 2020; published online 25 September 2020. Copyright © 2020 by Kelsey H. Elfering and Kenneth O. Granlund. Published by the American Institute of Aeronautics and Astronautics, Inc., with permission. All requests for copying and permission to reprint should be submitted to CCC at [www.copyright.com](http://www.copyright.com); employ the eISSN 1533-385X to initiate your request. See also AIAA Rights and Permissions [www.aiaa.org/randp](http://www.aiaa.org/randp).

\*Graduate Research Assistant, Department of Aerospace and Mechanical Engineering; [kelferi@ncsu.edu](mailto:kelferi@ncsu.edu). Student Member AIAA.

†Assistant Professor, Department of Aerospace and Mechanical Engineering; [kgranlu@ncsu.edu](mailto:kgranlu@ncsu.edu). Associate Fellow AIAA.

incompressible, single-blade, and oscillatory planar motions. These characteristics are often modified due to too many variables affecting the same physical mechanisms of the results. There is a base of existing works that have taken a similar approach, but often have investigated either a singular motion of surge, pitch, or plunge, or a combination of two motions, but less frequency of all three motions combined. An earlier representative experimental work of pure surge investigations can be found in [1] and more recently in [2,3]. Of key interest has been the interaction of pitch and plunge, as the linear superposition of both lift forces has been thought to be nearly equal to one another [4–8]. There are also example works that investigated coupling of surge–pitch in [9–11], and also Choi et al. [12] investigated surge–plunge coupling. An example of investigating all three motions can be found in [13] concerning recreation of gust effects. This work proposes to investigate this simplified case for two-dimensional, unsteady aerodynamics of a single, rigid airfoil undergoing planar oscillatory motion of the combined motions of surge, pitch, and plunge.

The notable work of Greenberg [14] has influenced this research area greatly as a closed-form solution to an airfoil undergoing small, sinusoidal oscillations of surge, pitch, and plunge. With Greenberg's lift equation, a phase shift is introduced between the sinusoidal combinations of surge, pitch, and plunge to determine the airfoil normalized lift with the aim of canceling dynamic lift effects. The required phase shift and corresponding variables related to these motions are determined analytically and verified experimentally to obtain lift equivalence between pitch and plunge to cancel surge and the respective coupled terms of surge–pitch and surge–plunge.

## II. Background

Here, we use reduced frequency  $k$  to describe the angular wave-number of shed vorticity from the trailing edge. If  $k \rightarrow 0$ , the shed vorticity from a change in the state of circulation of the airfoil has advected far enough downstream in the wake that it does not influence the instantaneous circulation of the airfoil; we call this quasi steady. When  $k > 1$  and the amplitude of unsteady motion is small, noncirculatory effects start to dominate. In the range of  $k = O(0.1)$  is where the effects of wake circulation are largest.

Theodorsen's solutions [15] were built with a time domain created by Wagner [16] to predict wing and airfoil behavior. Isaacs [17] extended Theodorsen's theory to include a periodic, sinusoidal free-stream velocity with a fixed pitch about the midchord, excluding plunge, with a Fourier series describing the wake. The Theodorsen approach was used toward pitch–plunge lift-based equivalence and cancellation by McGowan et al. [4]. The basis for this equivalence process is a starting point for the added complexity of introducing surge to the equation.

When surge is a component of the Greenberg equations, coupling interactions occur between surge–pitch and surge–plunge, which is a departure from the linear superposition that occurs between pitch–plunge. Greenberg [14] used both theories to introduce a closed-form, analytical result to include harmonic plunge and pitch motions to predict lift and pitching moment in an oscillating freestream. This allowed for changes in motion, like surge rate to be included instead of strictly using constant incidence and resulted in a simpler equation for implementation.

Van der Wall and Leishman [18] evaluated multiple theories in comparison to Isaacs [17], one being the Greenberg theory [14]. The thorough review demonstrates that Greenberg's theory assumes a uniform velocity perturbation following the chord of a flat plate in potential flow. This describes a back-and-forth motion into and away from the freestream and not necessarily an oscillating freestream velocity. Another simplification is that a high frequency is applied to the wake integrals to result in constantly spaced, periodic wake structures and concluded that this is equal to neglecting the induced velocity flow oscillation amplitude and makes the theory substantially inaccurate above  $\sigma = 0.4$  [18].

Granlund et al. [2] also demonstrated that moving a test article in a constant freestream yields a similar result to an oscillating freestream with a static test article, a finding that allows for a test article motion methodology to be conducted for predicting streamwise gusts as

well. These oscillating freestream experiments were conducted in a shuttered wind tunnel that can produce sinusoidal variation up to 10% independent of frequency  $k < 2.5$ .

These theories are meant to predict the unsteady behavior of airfoils while the flow remains attached, without reverse flow, and with small dynamic motions. Because of the range and rate of dynamic airfoil motions, separation of the boundary layer from the airfoil occurs. This led to several experimental investigations [4,5] to determine if the equations still predicted lift accurately when separation occurs.

More recently, Greenblatt et al. [3] varied flow speed in a wind tunnel test section with moving louvers at Reynolds number 75,000 and 125,000 for NACA 0012 and 0018 airfoils. This shuttered wind tunnel testing method produces a gust for velocity oscillation and a pressure gradient in the freestream direction. The gust couples the reduced frequency  $k$  to the oscillation amplitude  $\sigma$  compared with the freestream velocity, but only select combinations of parameters exist because the large oscillation amplitude is achieved by operating the tunnel in resonance [19]. Results indicated that there was not strong coupling between the simultaneous oscillation of pitching and surging. This finding lends to only include the primary coupling modes between surge and pitch in the following lift equivalence model.

Finding a lack of high-amplitude oscillating freestream comparison to these theories, Strangfeld et al. [9] evaluated surge amplitude up to  $\sigma = 0.5$  and  $k$  of 0.074–0.0985 for a NACA 0018, mean Reynolds number of 300,000, at constant, different, positive, and negative static angles of attack of 1, 2, 3, 4, and 8 deg. They concluded that separation bubble location on the airfoil suction surface and breakdown of the Kutta condition causes Greenberg and other theories to be inapplicable to thick airfoils below Reynolds number 1,000,000.

A general consensus is that the linearized assumption in the Greenberg equation is most relevant when separation only occurs from the trailing edge, because the bound circulation in the theory is shed here due to the Kutta condition [9,18]. This physical constraint is a primary reason that a thicker NACA 0018 airfoil was chosen to promote trailing edge separation.

In the current work, combinations of surge–pitch–plunge at Reynolds number 40,000 for a NACA 0018 airfoil are studied using an analytical Greenberg [14] method and experimental mean force measurements with dye-flow visualization in a free-surface water tunnel [20]. In this approach, the theory is compared with experiment while observing the flow conditions as they conform and deviate from the theoretical assumptions.

## III. Analytical Approach to Surge–Pitch–Plunge Equivalence and Cancellation

The pitch amplitude is varied with the pivot-point location at the quarter-chord. The corresponding equivalent pure pitch and plunge amplitudes with phase shift  $\Psi$  are determined from the lift-based equivalence method of the Theodorsen theory [4,15]. These findings due to the linear superposition of pitch and plunge are leveraged and applied toward the Greenberg theory [14]. The initial Greenberg theory approach begins with only considering the two translating oscillations of surge and plunge. This is accomplished by introducing a phase shift  $\phi$  between surge and plunge while temporarily omitting the pitch terms. Once  $\phi$  is determined, the lift terms due to pitch are reintroduced with the phase shift between surge and pitch represented as  $\Psi + \phi$ . This phase shift result is a commutative bridge between pitch–plunge and surge–plunge that now relates surge–pitch, and relates a complete phase shift theory between surge, pitch, and plunge.

### A. Theodorsen Theory

In this section, the McGowan approach [4] for pitch–plunge equivalence is revisited. Phase shift and amplitude for pitch–plunge equivalence requires the lift for plunge be set equal to pitch. The lift due to Theodorsen's theory solely for airfoil unsteady pitch–plunge contributions is

$$L_t(t) = -\pi\rho b^2(\ddot{h} + v_0\dot{\theta} - \pi b a\ddot{\theta}) - 2\pi\rho v_0 C(k) \left( \dot{h} + v_0\theta + b\left(\frac{1}{2} - a\right)\dot{\theta} \right) \quad (1)$$

The plunge and pitch displacements are denoted by  $h$  and  $\theta$ , respectively, to match the parts of vertical displacement and angle of attack, where the amplitudes are  $h_m$  and  $\theta_m$ . These terms are for continuity of nomenclature when Theodorsen's theory is represented in the later Greenberg approach. The pivot point for pitch along the chordwise distance from the leading edge is  $x_p$ , where the half chord is  $b$  and the pivot point  $a = (x_p - b)/b$ . With a frequency  $f$  and period  $T$  the circular frequency is defined as  $\omega = 2\pi f$  and the reduced frequency is  $k = \omega b/V_\infty$ . For pure-sinusoidal motions, the plunge displacement, plunge velocity, and plunge acceleration are

$$h = h_m e^{i\omega t} \quad \dot{h} = h_m i\omega e^{i\omega t} \quad \ddot{h} = -h_m \omega^2 e^{i\omega t} \quad (2)$$

With pitch, pitch rate, and pitch acceleration as follows, where  $\Psi$  is a phase angle:

$$\theta = \theta_m e^{i(\omega t + \Psi)} = \theta_m e^{i\omega t} e^{i\Psi} \quad \dot{\theta} = \theta_m i\omega e^{i(\omega t + \Psi)} = \theta_m i\omega e^{i\omega t} e^{i\Psi} \\ \ddot{\theta} = -\theta_m \omega^2 e^{i(\omega t + \Psi)} = -\theta_m \omega^2 e^{i\omega t} e^{i\Psi} \quad (3)$$

The expressions for  $h$  and  $\theta$  and their respective time derivatives from Eqs. (2) and (3) are substituted into the lift Eq. (1) and arranged such that  $L_{t,\text{plunge}}(t) = L_{t,\text{pitch}}(t)$ . The McGowan solution to the Theodorsen pitch–plunge lift-based equivalence equations for pitch phase shift (6), and pitch–plunge amplitudes (4) and (5), for a given reduced frequency yields the real parts followed by the imaginary parts:

$$h_m E = (C \cos \Psi - B \sin \Psi) \theta_m \quad (4)$$

$$-h_m D = (B \cos \Psi + C \sin \Psi) \theta_m \quad (5)$$

The closed-form solution for the phase shift angle  $\Psi$  is found as the following expression when Eq. (4) is divided by Eq. (5) and dividing the resulting expression right-hand-side numerator and denominator by  $\cos \Psi$ .

$$\Psi = \tan^{-1} \left( \frac{C - AB}{AC + B} \right) \quad (6)$$

where

$$A = (k + 2G)/(-2F) \quad B = k + 2G + 2k \left( \frac{1}{2} - a \right) F$$

$$C = ak^2 + 2F - 2k \left( \frac{1}{2} - a \right) G$$

Additionally defined

$$D = 2 \frac{k}{b} F \quad E = \frac{k}{b} (k + 2G)$$

Consider the case of pitch–plunge with a reduced frequency of 0.393 and a plunge amplitude (with respect to chord length) of  $0.50c$  shown in Fig. 1. From Eq. (4) this yields a pitch amplitude of  $19.91^\circ$  and a pitch phase shift of  $69.82^\circ$  from Eq. (6). Lift equivalence and cancellation are achieved by determining identical pitch–plunge amplitudes and corresponding phase shift angle, and there is time-independent linear superposition between the two lift components. It is noted that the phase angle and pitch–plunge amplitude relationships are only dependent on the reduced frequency, pivot-point location, and the Theodorsen function  $C(k)$ .

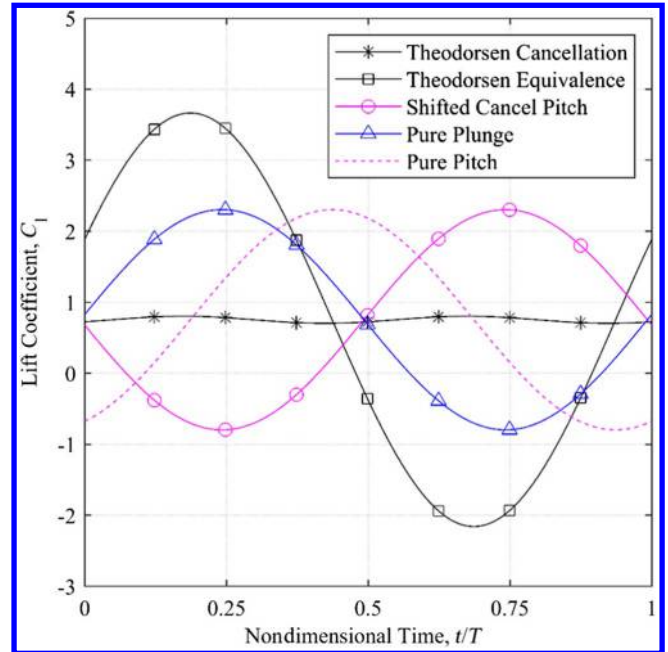


Fig. 1 Recreated example case 3E, of the McGowan  $C_{l_t}(t/T)$  solution [4] of the Theodorsen lift-based equivalence and cancellation for  $k = 0.393$ ,  $\theta_m = 19.91^\circ$ ,  $h_m = 0.50c$ ,  $\sigma = 0$ ,  $\Psi = 69.82^\circ$ .

## B. Greenberg Surge–Plunge Theory

Linear superposition between all lift components does not occur when a surge element is present in the cases of surge–pitch, surge–plunge, or surge–pitch–plunge. A formulation of the same method that was employed to find Eqs. (4–6) is considered for a reduced Greenberg surge–plunge equation. A new phase shift angle  $\phi$  is introduced between surge and plunge lift components, where the plunge displacement, plunge velocity, and plunge acceleration become

$$h = h_m e^{i(\omega t + \phi)} = h_m e^{i\omega t} e^{i\phi} \\ \dot{h} = h_m i\omega e^{i(\omega t + \phi)} = h_m i\omega e^{i\omega t} e^{i\phi} \\ \ddot{h} = -h_m \omega^2 e^{i(\omega t + \phi)} = -h_m \omega^2 e^{i\omega t} e^{i\phi}$$

$$L_{g,\text{surge-plunge}}(t) = -\pi\rho b^2[\ddot{h} + \dot{v}\theta_m] - 2\pi\rho v b[v_0\theta_m + \sigma v_0\theta_m C(k)e^{i\omega t} + \dot{h}C(k)] \quad (7)$$

where

$$v = v_0(1 + \sigma e^{i\omega t}) \quad \dot{v} = i v_0 \sigma \omega e^{i\omega t} \quad (8)$$

Equation (7) is a reduced surge–plunge Greenberg expression for lift. The surge velocity and acceleration are left in complex form defined in Eq. (8). For surge–plunge equivalence, the pure plunge component is set equal to the pure surge and surge–plunge coupled components. The expressions for plunge displacement  $h$  and respective derivatives are substituted into Eq. (7) and arranged, where  $L_{g,\text{plunge}}(t) = L_{g,\text{surge}}(t) + L_{g,\text{surge-plunge,coupled}}(t)$ . Equations (9) and (10) yield the real part relationships followed by the imaginary parts.

$$\sigma\theta_m(L + 2) = h_m \frac{k}{b} (K \cos \phi - L \sin \phi) \quad (9)$$

$$\sigma\theta_m K = h_m \frac{k}{b} (L \cos \phi + K \sin \phi) \quad (10)$$

where

$$K = -k - 2G - 2\sigma G \cos \omega t - 2\sigma F \sin \omega t$$

$$L = 2F + 2\sigma F \cos \omega t - 2\sigma G \sin \omega t$$

The phase shift angle  $\phi$  closed-form solution is found as the following expression when Eq. (9) is divided by Eq. (10) and dividing the resulting expression right-hand-side numerator and denominator by  $\cos \phi$ .

$$\phi = \tan^{-1} \left( \frac{K^2 + L^2 + 2L}{2K} \right) \quad (11)$$

Here it is noted that the phase shift and surge–plunge relationship are time dependent, which would require a time-varying angle of attack. To meet a dynamic angle of attack, inherently a pitching motion element would have to be introduced to satisfy this constraint, eliminating the potential of solely having surge–plunge motions for lift-based equivalence and cancellation. These expressions would also result in a nonsinusoidal oscillation motion with a time-dependent phase shift angle. It is due to these reasons that equivalence and cancellation for the Greenberg theory with a surge component require all three motions of surge–pitch–plunge.

### C. Greenberg Surge–Pitch–Plunge Theory

If only pitch and plunge occurred without surge amplitude, the Greenberg equation [14] does not simplify to the Theodorsen equation, the last term in Eq. (12) being the differentiation. The Greenberg lift equation is

$$\begin{aligned} L_g(t) = & -\pi\rho b^2[\ddot{h} + v\dot{\theta} + \dot{v}(\theta_m + \theta) - ab\ddot{\theta}] \\ & - 2\pi\rho vb[v_0\theta_m + \sigma v_0\theta_m C(k)e^{i\omega t} + (b(1/2 - a)\dot{\theta} + v_0\theta)C(k) \\ & + \dot{h}C(k) + v_0\theta C(2k)e^{i\omega t}] \end{aligned} \quad (12)$$

The analytical approach presented here removes the last term so that when the surge amplitude is zero the Greenberg theory reduces to the Theodorsen theory. Consideration is also taken for the surge–pitch coupling from this term to be neglected due to the findings of Greenblatt et al. [3]; there was not strong coupling between the simultaneous oscillation of pitching and surging. This reduction yields

$$\begin{aligned} L_{g,\text{reduced}}(t) = & -\pi\rho b^2[\ddot{h} + v\dot{\theta} + \dot{v}(\theta_m + \theta) - ab\ddot{\theta}] \\ & - 2\pi\rho vb[v_0\theta_m + \sigma v_0\theta_m C(k)e^{i\omega t} \\ & + (b(1/2 - a)\dot{\theta} + v_0\theta)C(k) + \dot{h}C(k)] \end{aligned} \quad (13)$$

Now that the surge–plunge phase angle  $\phi$  has been determined in the previous section, and the lift terms due to pitch have been reintroduced to the lift equation, the phase shift between surge and pitch is represented as  $\Psi + \phi$ . This phase shift is a commutative bridge between pitch–plunge and surge–plunge that now relates surge–pitch, completing the phase shift relationship between surge–pitch–plunge. The plunge displacement parameters are maintained from Eq. (7) and the pitch, pitch rate, and pitch acceleration are

$$\begin{aligned} \theta &= \theta_m e^{i(\omega t + \Psi + \phi)} = \theta_m e^{i\omega t} e^{i(\Psi + \phi)} \\ \dot{\theta} &= \theta_m i\omega e^{i(\omega t + \Psi + \phi)} = \theta_m i\omega e^{i\omega t} e^{i(\Psi + \phi)} \\ \ddot{\theta} &= -\theta_m \omega^2 e^{i(\omega t + \Psi + \phi)} = -\theta_m \omega^2 e^{i\omega t} e^{i(\Psi + \phi)} \end{aligned} \quad (14)$$

With prescribed pitch and plunge amplitudes from the Theodorsen theory and the phase shift angles determined in the previous sections, the aim is to determine a surge amplitude  $\sigma$  that results in lift cancellation with the best agreement to constant freestream velocity and incidence angle. The best agreement is defined as the lowest change in lift, through root-mean-squared error (RMSE) with respect to the static lift. The expressions for  $h$  and  $\theta$  and their respective time derivatives from Eqs. (7) and (14) are substituted into the lift Eq. (13) and arranged where  $L_{g,\text{pitch}}(t) + L_{g,\text{plunge}}(t) = L_{g,\text{surge}}(t) + L_{g,\text{surge-plunge,coupled}}(t) + L_{g,\text{surge-pitch,coupled}}(t)$ . The result of the real parts followed by the imaginary parts are

$$\begin{aligned} & \theta_m [C \cos(\Psi + \phi) - B \sin(\Psi + \phi)] - h_m [E \cos \phi + D \sin \phi] \\ &= \sigma \theta_m (L + 2) - \sigma \theta_m [(S \cos \omega t + R \sin \omega t) \cos(\Psi + \phi) \\ &+ (R \cos \omega t - S \sin \omega t) \sin(\Psi + \phi)] \\ &- \sigma h_m [(H \cos \omega t + D \sin \omega t) \cos \phi + (D \cos \omega t - H \sin \omega t) \sin \phi] \end{aligned} \quad (15)$$

$$\begin{aligned} & \theta_m [B \cos(\Psi + \phi) + C \sin(\Psi + \phi)] + h_m [D \cos \phi - E \sin \phi] \\ &= -\sigma \theta_m K - \sigma \theta_m [(-R \cos \omega t + S \sin \omega t) \cos(\Psi + \phi) \\ &+ (S \cos \omega t + R \sin \omega t) \sin(\Psi + \phi)] \\ &+ \sigma h_m [(D \cos \omega t + H \sin \omega t) \cos \phi + (H \cos \omega t + D \sin \omega t) \sin \phi] \end{aligned} \quad (16)$$

where the following coefficients have been maintained from the Theodorsen theory section:

$$\begin{aligned} B &= k + 2G + 2k \left( \frac{1}{2} - a \right) F & C &= ak^2 + 2F - 2k \left( \frac{1}{2} - a \right) G \\ D &= 2 \frac{k}{b} F & E &= \frac{k}{b} (k + 2G) \end{aligned}$$

Additionally, the following coefficients are maintained from the Greenberg surge–plunge theory:

$$\begin{aligned} K &= -k - 2G - 2\sigma G \cos \omega t - 2\sigma F \sin \omega t \\ L &= 2F + 2\sigma F \cos \omega t - 2\sigma G \sin \omega t \end{aligned}$$

The new coefficients introduced to this section are

$$H = 2 \frac{k}{b} G \quad R = k(1 + \theta_m) + (1 - 2a)kF + 2G \quad S = (1 - 2a)kG - 2F \quad (17)$$

The surge-related components have been kept on the right-hand side of Eqs. (15) and (16) to demonstrate that when the surge amplitude is equal to zero,  $\sigma = 0$ , the right-hand sides are equal to zero. This eliminates the need for a surge–plunge phase angle relationship setting  $\phi = 0$ . This reduces Eqs. (15) and (16) to Eqs. (4) and (5) when the remaining pitch contributions are subtracted to the right-hand side. When  $\sigma = 0$ ,

$$\begin{aligned} & \theta_m [C \cos(\Psi + \phi) - B \sin(\Psi + \phi)] - h_m [E \cos \phi + D \sin \phi] = 0 \\ & \theta_m [B \cos(\Psi + \phi) + C \sin(\Psi + \phi)] + h_m [D \cos \phi - E \sin \phi] = 0 \end{aligned}$$

And with  $\phi$  eliminated, setting  $\phi = 0$ ,

$$\begin{aligned} & \theta_m [C \cos(\Psi + 0) - B \sin(\Psi + 0)] - h_m [E \cos(0) + D \sin(0)] = 0 \\ & \theta_m [B \cos(+0) + C \sin(\Psi + 0)] + h_m [D \cos(0) - E \sin(0)] = 0 \end{aligned}$$

Observing that  $\cos(0) = 1$  and  $\sin(0) = 0$ , and rearranging, Eqs. (15) and (16) reduce to Eqs. (4) and (5):

$$\begin{aligned} h_m E &= (C \cos \Psi - B \sin \Psi) \theta_m \\ -h_m D &= (B \cos \Psi + C \sin \Psi) \theta_m \end{aligned}$$

Further observation of Eqs. (15) and (16) shows that there are surge amplitude parameters that are contained in the  $K$  and  $L$  coefficients that are second-order surge amplitude contributions. With  $K$  and  $L$  expanded and the left-hand side of Eqs. (15) and (16) moved to the right-hand side as a consequence of the equivalence method, the real and imaginary parts take the form of a quadratic equation with  $\sigma$  as the quadratic variable:

$$\begin{aligned} & \sigma^2 \theta_m (2F \cos \omega t - 2G \sin \omega t) \\ & - \sigma \theta_m (-2F - 2 + (S \cos \omega t + R \sin \omega t) \cos(\Psi + \phi)) \\ & + (R \cos \omega t - S \sin \omega t) \sin(\Psi + \phi) - \sigma h_m [(H \cos \omega t + D \sin \omega t) \cos \phi \\ & + (D \cos \omega t - H \sin \omega t) \sin \phi] + \theta_m [C \cos(\Psi + \phi) - B \sin(\Psi + \phi)] \\ & - h_m [E \cos \phi + D \sin \phi] = 0 \end{aligned} \quad (18)$$

$$\begin{aligned} & \sigma^2 \theta_m (2G \cos \omega t + 2F \sin \omega t) \\ & - \sigma \theta_m (-k - 2G + (-R \cos \omega t + S \sin \omega t) \cos(\Psi + \phi)) \\ & + (S \cos \omega t + R \sin \omega t) \sin(\Psi + \phi) + \sigma h_m [(D \cos \omega t + H \sin \omega t) \cos \phi \\ & + (H \cos \omega t + D \sin \omega t) \sin \phi] + \theta_m [B \cos(\Psi + \phi) + C \sin(\Psi + \phi)] \\ & + h_m [D \cos \phi - E \sin \phi] = 0 \end{aligned} \quad (19)$$

Solving the quadratic equation (written in terms of  $x$ ,  $y$ , and  $z$ , as  $a$ ,  $b$ , and  $c$  are already disposed) for Eq. (18) in terms of  $\sigma$ , where

$$\begin{aligned} x &= \theta_m (2F \cos \omega t - 2G \sin \omega t) \\ y &= -\theta_m (-2F - 2 + (S \cos \omega t + R \sin \omega t) \cos(\Psi + \phi) \\ & + (R \cos \omega t - S \sin \omega t) \sin(\Psi + \phi)) - \sigma h_m [(H \cos \omega t + D \sin \omega t) \cos \phi \\ & + (D \cos \omega t - H \sin \omega t) \sin \phi] \\ z &= \theta_m [C \cos(\Psi + \phi) - B \sin(\Psi + \phi)] - h_m [E \cos \phi + D \sin \phi] \\ \sigma &= \frac{(-y \pm \sqrt{y^2 - 4xz})}{(2x)} \end{aligned} \quad (20)$$

A more time-intensive numeric RMSE minimization analysis to determine the optimal surge amplitude for Eq. (13) is undertaken to compare to the analytic solution of Eq. (20). The numeric solution is achieved by sweeping through the surge amplitude for the range of 0.0–1.0 and determining the RMSE of the lift as it compares to the static lift case. The result is shown in Fig. 2 with good agreement between the analytical, real positive root, and numerical solution. The numeric solution also shows that there is a relatively flat portion of the curve, referred to as a robust zone, for the range of surge amplitudes

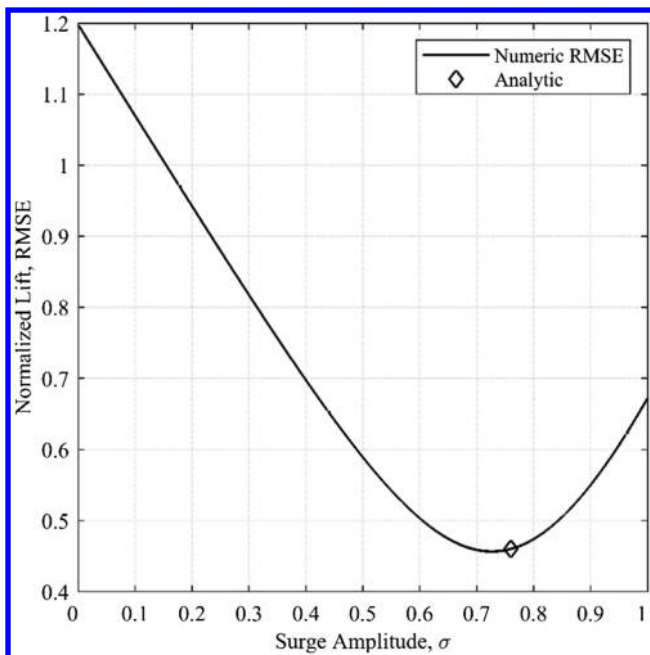


Fig. 2 An example finding of Eq. (13), minimum RMSE for a numeric surge sweep and Eq. (20), an analytic solution for  $k = 0.10$ ,  $\theta_m = 3.0^\circ$ ,  $h_m = 0.263c$ ,  $= 0$  to 1,  $\Psi = 84.28^\circ$ ,  $\phi = 85.99^\circ$ .

equal to 0.60–0.85, where the RMSE change is less than 10% from the local minima.

The surge component of the reduced Greenberg lift Eq. (13) is treated as the reference motion that plunge and pitch are phase shifted from. The surge abscissa in this formulation and experiments are zero when the airfoil motion has been located in the typical manner where the airfoil motion just begins to surge and advances into the flow at  $t/T = 0.0$ , followed by the motion retreat, surging away from the flow starting at  $t/T = 0.5$ . The static lift components have been included in the total lift equivalence and cancellation cases in Fig. 3, but have been left out of the individual component contributions to show the construction and destructive interferences to visualize the mean ordinate as zero. Figure 3 includes the individual components of Eq. (13) as well as the combination of those components represented by the overall lift,  $L_{g,\text{reduced}}(t)$ .

The maximum dynamic lift from the left of Fig. 3, at a temporal 0.264, when compared with the same time of the right of Fig. 3 is over 90% negated in terms of dynamic deviation from static lift. The remaining deviation from static lift is due to a couple of reasons. First, the surge component is not purely sinusoidal, where the pure plunge and pitch components are. This creates a need for compromise between determining the surge magnitude factor for cancellation to occur at both maximum and minimum surge lift values.

Secondly, at a lower lift magnitude scale, there is a small phase shift between the surge–pitch and surge–plunge coupled components. The pitch–plunge equivalence in opposition to surge was chosen due to pitch and plunge having an identical frequency to surge, as well as larger magnitude than the coupled surge–pitch and surge–plunge elements for  $\sigma < 1$ . This similarly has a positive lift amplitude effect for equivalence, where both pitch and plunge are each approximately half the amplitude of surge. This maximizes the positive sinusoid construction when constrained by the same parameters used for cancellation.

#### D. Quasi-Steady Normalized Lift

Van der Wall and Leishman's [18] evaluation of the Greenberg theory [14] presented the assumptions that neglected the induced velocity flow oscillation amplitude and describe a back-and-forth motion into and away from the freestream. That does not necessarily represent an oscillating freestream velocity and creates substantial inaccuracies above  $\sigma = 0.4$ . Based on these assumptions a dynamic pressure correction in the direction of the flow may correlate the differences between analytical theories to the experimental results more accurately. A Reynolds number of 40,000 is low when considering an airfoil, resulting in high influence of Reynolds number effect and thick airfoil effects on lift. A separation bubble or separation location (leading edge, midchord, or trailing edge) plays a leading role in airfoil lift production for low Reynolds numbers in unsteady flows [6,21].

The lift is normalized by static lift to observe the lift produced by the unsteady combined motions. The lift may also be normalized by the Greenberg lift as the unsteadiness goes to zero. This is a quasi-steady normalization that allows the unsteadiness of the lift to be quantified. In the work of Van der Wall and Leishman [18], Theodorsen's theory is extended to also have a periodic freestream velocity. This assumed a constant shed wake velocity relative to the airfoil and omits any time-varying effects from the wake integrals. The normalized quasi-steady term from Van der Wall and Leishman for the extended periodic freestream Theodorsen theory is Eq. (21).

$$\frac{L_{qs}(t)}{L_0} = (1 + \sigma \sin \omega t)^2 \quad (21)$$

These assumptions are analogous to  $k \rightarrow 0$ ,  $F(k) \rightarrow 1$ , and  $G(k) \rightarrow 0$ . If these assumptions are applied to the reduced Greenberg theory, Eq. (13), the result is Eq. (22).

$$\begin{aligned} \frac{L_{q,s,g}(t)}{L_0} &= (\sigma^2 + \sigma \theta_m)(\cos 2\omega t + i2 \cos \omega t \sin \omega t) \\ &+ (2\sigma + \theta_m)(\cos \omega t + i \sin \omega t) + 1 \end{aligned} \quad (22)$$

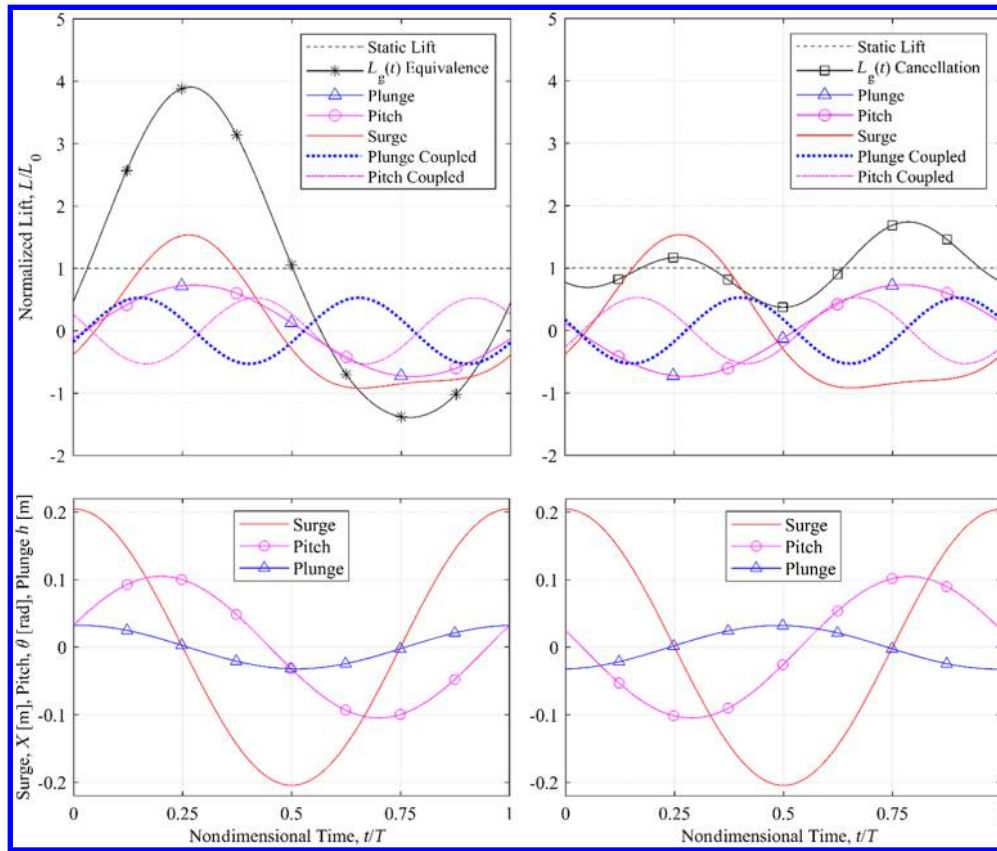


Fig. 3 Normalized lift, equivalence (top left) and cancellation (top right), theory analytics for lift components of  $k = 0.25$ ,  $\theta_m = \pm 6.0^\circ$ ,  $h_m = \pm 0.221c$ ,  $\Psi = 76.16^\circ$ ,  $\phi = 85.40^\circ$ ,  $\sigma = 0.7$ . Followed by kinematics of equivalence (bottom left) and cancellation (bottom right).

When the pitch amplitude  $\theta_m$  is set to zero and the real components of Eq. (22) are considered after simplification (with the result shifted right by  $\pi/2$  to conform to the typical abscissa described above), Eq. (22) simplifies to Eq. (21). If the pitch amplitude is neglected, then the normalized quasi-steady Eq. (21) is also valid for the Greenberg theory.

If  $\theta_m$  is not set to zero, the result of Eq. (22) shifted right by  $\pi/2$  to conform to the typical abscissa with only the real parts considered, Eq. (22) becomes Eq. (23).

$$\frac{L_{q,g}(t)}{L_0} = -(\sigma^2 + \sigma\theta_m) \cos 2\omega t + (2\sigma + \theta_m) \sin \omega t + 1 \quad (23)$$

This expression becomes increasingly complicated when a phase shift in pitch is considered. When investigated, it was observed that neither Eq. (23), nor a pitch phase shift consideration changed the trends of a quasi-steady normalization of the lift. It is also noted that unlike the translational velocities of surge and plunge, pitch rate does not change each chord element location at the same velocity, as each chordwise position changes distance from the pivot location. However, as  $k \rightarrow 0$ , for the quasi-steady case, the pitch rate and acceleration are also zero, limiting the significance of a change in rotation along the chord.

The normalized quasi-steady lift in Eq. (21) is maintained as being useful in demonstrating unsteadiness through the quasi-steady normalization of lift. A value of one indicates that the airfoil is behaving as if it were steady. Above one indicates that the unsteadiness is increasing lift production, and below one indicates that the unsteadiness is decreasing lift compared with a static lift case at constant freestream and incidence angle. The normalized lift by quasi-steady lift becomes Eq. (24).

$$\frac{L_g(t)}{L_{qs}(t)} = \frac{L_g(t)}{L_0} \frac{L_0}{L_{qs}(t)} = \frac{L_g(t)}{L_0} \frac{1}{(1 + \sigma \sin \omega t)^2} \quad (24)$$

## IV. Experimental Setup

The experimental setup method is designed to meet the unsteady aerodynamic characterization of the flowfield through dye tracking visualization, as well as load quantification through load cell lift and pitching moment histories. This was accomplished with the following motion system method and experimental techniques.

### A. Water Tunnel

The experimental equipment employed to create and measure unsteady aerodynamics was conducted with a free-surface water tunnel at the North Carolina State University. The water tunnel contains approximately 13,250 liters of water at 0.61 m water height. Freestream velocity is generated by a marine propeller housed in a pipe under the test section. The propeller is powered by a 10 HP Baldor Reliance Super E Motor EM3774T controlled by an ABB ACS355 variable frequency drive. The water is propelled through the diffuser and settling chamber through progressive turbulence screens and accelerated through the contraction into the test section.

The test section length of 2.44 m is long enough for motion inputs of low reduced frequencies,  $k = 0.05$  and  $\sigma = 0.5$ . The leveraged advantage of a water tunnel is that  $k$  and  $\sigma$  are independent variable inputs at this facility. Conversely, these parameters for a shuttered wind tunnel are coupled and cannot be treated individually. For an equivalent Reynolds number comparison, with only surging motions considered, the airfoil motion would need to be faster at much greater motion amplitudes in a wind tunnel compared to a water tunnel. Although not impossible, this would be difficult and limit the range of reduced frequencies greatly. These differences allow for more ease in camera tracking of the test article for dye visualization as well as a greater range of cases.

The water tunnel test section is constructed of three glass panels with dimensions for the two vertical sides of 0.71 m height by 2.44 m length and a floor panel of 0.81 m width by 2.44 m length. There is unobstructed viewing through the glass panels throughout the test section for optical measurements. A 4.5:1 contraction produces free-stream velocities from 0.15 to 1.0 m/s with the average streamwise

turbulence varying from 0.2% to 0.8%, increasing proportionally with freestream velocity [20].

## B. Motion System

The tunnel is equipped with a H2 W motion system controlled by a Galil 4080 controller and Xenus XTL-230-36 amplifiers operated using Galil Suite software. Custom programs downloaded into the controller determine the motions of the test article with respect to the freestream velocity. The controller uses the amplifiers to change magnetic fields on the various rails and rotary motor with location encoder feedback to meet the specified programmed motion for the experiment. If the motors exceed a given position tolerance, an error occurs and the test is stopped.

A dual-axis gantry denoted twice by "A" on the right in Fig. 4 is powered by two H2 W single rail linear stages. This dual-stage allows the test article to surge into and away from the freestream velocity as the flow exits the contraction from left to right. The gantry is placed 20 cm above the free surface water line and spans the entire length of the test section. The gantry has a maximum continuous output of 294 N and a peak output of 880 N.

Beneath the test section floor is a H2 W dual rail linear stage (DRS), denoted by "B," aligned with the centerline of the test section. The DRS rail system is designed where motion inputs of the test article can be tracked using cameras and other hardware during the specified motion. The DRS stage spans the entire length below the test section and has a continuous output of 44 N.

A second dual rail stage spans the width of the test section, denoted by "C," allowing the test article to plunge. The rotary motor, denoted by "D," allows the test article to pitch. The motion system uses RLS LM 13 linear magnetic encoders as feedback position sensors with a resolution of  $1\ \mu\text{m}$  for the linear rails and a rotary encoder with  $1/125$ th of a degree resolution for the rotary motor.

## C. Measurement and Data Acquisition Equipment

Experimental characterization techniques to measure the properties of unsteady aerodynamics employed are load cell mean force measurements, with respect to the quarter chord, and dye visualization.

The load cell is an ATI Industrial Automation Delta sensor to measure force and torque with calibrated limits of 660 N with  $1/8$  N resolution in both the  $X$  and  $Y$  directions, representing drag and lift, creating a plane parallel to the bottom of the test section. The torque calibration range is 60 N·m in all three Cartesian directions and is measured with a separate flexure than force with 16-bit DAQ, National Instruments, resolution. The load cell is the single point of connection between the rotary motor and the airfoil test article. The vertical orientation and single point of connection of the mounted airfoil cause the rotary motor limitation of 53 N·m to be the limiting torque magnitude. This was used to verify the maximum allowable applied forces to determine the maximum airfoil chord and pitch angle. This led to the load cell having been sized accordingly for a 0.146 m chord with  $20^\circ$  pitch maximum with single-axis overload conditions far exceeding the applied loads. This is a maximum static blockage of 6.4% that only momentarily occurs during dynamic motions.

One side of a six-axis load cell ATI Delta is mounted to the bottom of the rotary motor. The other side of the load cell is connected to the vertically oriented airfoil test article to measure aerodynamic forces and pitching moment.

The airfoil is constructed from two internal spanwise CFRP tubes approximately at  $1/3 \times$  chord and  $2/3 \times$  chord, supporting four wire-EDM stainless steel profiles at  $3/4 \times$  span,  $1/2 \times$  span,  $1/4 \times$  span, and the top. The bottom profile is made of chlorinated polyvinyl chloride (CPVC) to prevent scratching the glass during the mounting process. The skin of the airfoil is made of two layers of vacuum-molded glass-fiber reinforced plastic (GFRP).

Twenty-five cycles sampled at 1 kHz of each motion were recorded to measure an accurate sample representation for the load cell data collection. The first three and the last two cycles were not used to eliminate potential influence from initial startup and completion of the oscillations, resulting in 20 total used cycles and then filtered at 5 times the motion frequency using a fourth-order Chebyshev II low-pass filter in MATLAB. A tare of the system motion was performed to isolate the aerodynamic and noncirculatory forces. A parameter study of reduced frequency of 0.10–0.25 in increments of 0.05 was conducted for a 0.146 m chord and 4.2-aspect-ratio NACA 0018 airfoil.

An aspect ratio of approximately four has been used in several water tunnel facilities. Aspect ratio and other experimental factors such as gap effects, freestream turbulence, airfoil stiffness, and static blockage are not entirely accounted for in the present experiment and can vary broadly between experimental facilities. The experiment does take measures to minimize the influence of these factors, but the affects cannot be eliminated. The work of Visbal [22] is a clear demonstration of how these factors can affect the flowfield of the airfoil and corresponding force measurements.

The natural frequency of 5.4 Hz of the submerged airfoil assembly was determined through fast Fourier transform of the lift force signal when tapped with a soft mallet. The forcing frequency range of 0.06–0.15 corresponding to reduced frequency of 0.10–0.25 is over an order of magnitude less than the natural frequency of the airfoil, resulting in negligible airfoil bending.

The lowest value of  $k$ , 0.10, has been chosen to meet the surge amplitude limitations of approximately 0.70 as found in the theory analysis. The longitudinal airfoil displacement into and away from the flow is dependent on the surge amplitude and reduced frequency. The range of displacement is 0.0584–1.022 m corresponding to bounds of  $k$ , 0.25 and  $\sigma$ , 0.10, and  $k$ , 0.10 and  $\sigma$ , 0.70. This reduced frequency also remains relevant to the value of 0.10 that rotorcraft most experience, and for circulatory effects to be dominant. The pitch angle amplitudes have been chosen to explore attached flow, trailing edge separation, and leading-edge separation cases. Equivalent plunge depths are determined by the Theodorsen theory, and a sweep of surge amplitudes of 0.10–0.70 has been chosen. The maximum surge amplitude of 0.70 was chosen to be relevant to the values that represented the best cancellation while limiting the potential for reverse flow.

The dye visualization setup used multiple 10 V, 520 nm LED diodes to create a horizontal sheet that illuminates a 2D plane of the test section at half span of the airfoil wetted height. The beam path of the diodes produced a  $30^\circ$  planar light sheet with 520-G-2 lenses. This plane corresponds to the 0.33 m height of the leading-edge dye

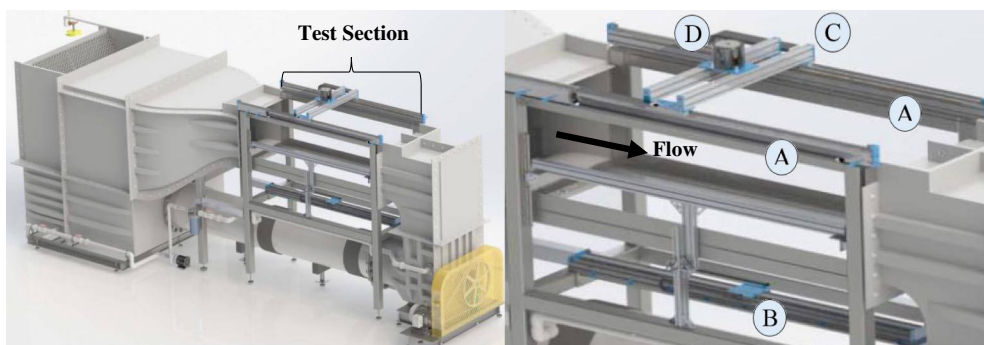


Fig. 4 Left: water tunnel model [20]. Right: test section with motion system rails and rotary motor.

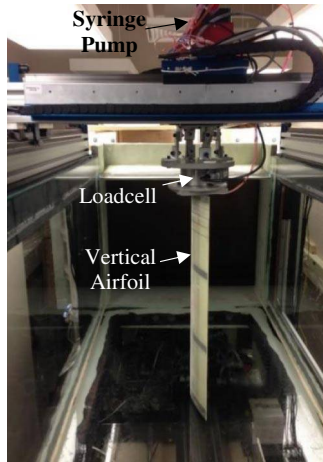


Fig. 5 Experimental NACA 0018 installed setup.

Table 1 Motion parameters

Case	$k$	$\theta_m$ , deg	$\Psi$ , deg	$h_m/c$	$\phi$ , deg	$\sigma$
A	0.10	3.00	84.282	0.264	85.75	0.10–0.70
B	0.10	4.00	84.282	0.352	85.75	0.10–0.70
C	0.10	6.00	84.282	0.528	85.75	0.10–0.70
D	0.10	8.00	84.282	0.704	85.75	0.10–0.70
E	0.15	3.00	81.472	0.178	85.40	0.10–0.70
F	0.15	4.00	81.472	0.237	85.40	0.10–0.70
G	0.15	6.00	81.472	0.356	85.40	0.10–0.70
H	0.15	8.00	81.472	0.474	85.40	0.10–0.70
I	0.20	3.00	78.748	0.135	85.60	0.10–0.70
J	0.20	4.00	78.748	0.180	85.60	0.10–0.70
K	0.20	6.00	78.748	0.271	85.60	0.10–0.70
L	0.20	8.00	78.748	0.361	85.60	0.10–0.70
M	0.25	3.00	76.156	0.110	86.72	0.10–0.70
N	0.25	4.00	76.156	0.147	86.72	0.10–0.70
O	0.25	6.00	76.156	0.221	86.72	0.10–0.70
P	0.25	8.00	76.156	0.294	86.72	0.10–0.70

port with a 1.082 mm diameter that ejects Rhodamine 6G from a New Era NE-300 syringe pump that fluoresces orange when exposed to this wavelength. The volumetric flow rate of dye was 3.50 mL/min, equating to 0.06 m/s velocity to be lower compared with the free-stream velocity so as not to disturb the boundary layer. The dye was mixed with half-and-half cream (density 1.02 kg/m<sup>3</sup>). As the airfoil is oscillated with given frequency and amplitude for a prescribed motion, the camera and airfoil follow the same simultaneous surge path to produce usable images at over 2 m in length for analysis.

The dye visualization simulates a 2D flow over the airfoil with the submerged wingtip of the airfoils within 1 mm of the test section floor. Mounted on the lower stage, as seen on the left of Fig. 5, below the test section is a Photron Mini AX200 high-speed camera with a Nikon NIKKOR 24 mm microlens. A Tiffen orange 21 filter is used with the dye visualization tracking with high-concentration Rhodamine-6G injection at 0.0041 g/mL, which fluoresces orange from the planar diode illumination shown in Fig. 6. Images are captured throughout the entire oscillation cycle of the motion as the camera track is simultaneously triggered and in synchronous motion with the longitudinal surging of the airfoil test article. A Keysight 33500B function generator simultaneously triggered the DMC motion controller and camera to synchronize the airfoil kinematics and dye visualization images. A Tektronix AGF 3022B function generator set the recorded camera frames per second (fps). Trigger delay is constrained by the motion controller by 2 ms, which is less than 11% of a phase angle of the fastest motion presented, and is considered negligible. Images of the motion are captured throughout the surging motion at 3 fps per phase angle using PFV Viewer software. The pitching and plunging motions are not matched by the camera system, where the images display the relative pitch–plunge motions between the camera system and the NACA 0018 test article.

## V. Results

A parameter study was considered for phase-shifted, sinusoidal surge–pitch–plunge for the NACA 0018 airfoil at a freestream, mean

Reynolds number of 40,000. Parameters that were chosen are reduced frequency  $k = 0.10$ – $0.25$  in increments of 0.05; pitch amplitude  $\alpha = 3, 4, 6,$  and  $8$  deg; and surge of  $\sigma = 0.10$ – $0.70$  in increments of 0.10. The corresponding plunge amplitudes were determined from the pitch amplitudes with the Theodorsen equivalence theory. Listed in Table 1 is a summary of the cases for equivalence. Table 1 represents cancellation as well, where  $h_m$  and  $\theta_m$  are the exact negative of the tabulated values. The mean angle of attack  $\alpha_m$  is always the positive value of  $\theta_m$ . The plunge phase shifts are an average value as this parameter is dependent on the surge amplitude. This was deemed to be acceptable as the plunge phase shift changed less than half of a degree within respective reduced frequency groups.

In this section, experimental comparison to theoretical predictions is made for normalized lift, and the discrepancies between the two are observed and related to dye visualization boundary layer and vortex shedding behavior. Inertial mass effects are subtracted from the load cell measurements and had a maximum normalized lift value of 0.025. This value corresponds to the maximum surge results of cases M–P, for  $k$  of 0.25 and  $\sigma$  of 0.70. The experiment is considered a viscous flow at a low, mean Reynolds number. As such, turbulent boundary layers, shear layer instability, leading-edge separation vortices, and even simultaneous, multiple-chordwise vortex roll-up and shedding occur. This is all in violation of the flat plate, potential flow with trailing edge Kutta condition enforcement that formulates the theory.

By enforcing the theoretical lift of the pitch and plunge amplitudes to always be equivalent, the total-lift theoretical predictions for surge–pitch–plunge are near identical for each pitch amplitude as reduced frequency increases from 0.1 to 0.25. As a consequence, the reduced frequency amplitude doubles the plunge displacement scales by approximately half, whereas the plunge rate remains nearly constant. This allowed for comparisons for each mean angle-of-attack group across reduced frequencies for their respective surge amplitudes while maintaining consistent theoretical predictions.

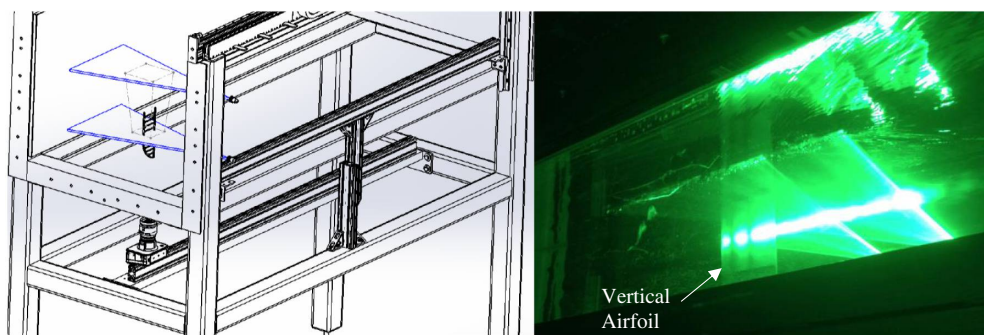


Fig. 6 Left: illumination design model [20]. Right: test section with airfoil and planar 520 nm illumination.

### A. Reduced Frequency and Surge Amplitude Trends

The deviations from a smooth, sinusoidal cycle for lower reduced frequencies in Fig. 7 are indicative of trends that occur throughout the parameter study investigated. At lower reduced frequencies, viscous separation effects and circulation are dominant, and allow more influence on the experimental lift when the Kutta condition is violated by boundary-layer separation and vortex roll-up that is followed by shedding. As the reduced frequency increases over the test range of 0.10–0.25, the circulatory effects become less dominant as the experimental results are influenced more by noncirculatory effects. This interaction results in lift behavior less influenced by boundary-layer attachment.

The influence of surge amplitude changes the strength and structure of these viscous effects as the dynamic pressure rate changes due to an increased motion frequency with respect to the freestream velocity. An absence in high surge amplitude findings was observed by Strangfeld et al. [9], testing to  $\sigma$  of 0.5. The analytical results indicated a maximum cancellation occurring at approximately 0.7, which motivates the discussion of the effect of the range of surge amplitudes in Fig. 8.

Figure 8 shows a time lapse of a cancellation case corresponding to the normalized lift shown in Fig. 9b, with constant parameters for each column, except for surge amplitude. The columns from left to right show surge amplitude of  $\sigma = 0.1, 0.4,$  and  $0.7$ . The horizontal lines in Fig. 8 denote a vertical plunge displacement reference datum for each airfoil dye visualization image for an overall amplitude  $h_m$  of  $0.356c$ . The nondimensionalized time shown is a single, ensemble-averaged period, where the force and motion are cyclic and time 0.000 is equal to time 1.000. The first three cycles are omitted to ensure that startup conditions have past before the images are recorded.

The changes due to surge amplitude are most apparent in the wake structure and height when investigating times near the peak motion deviations, as well as the separation location as the instantaneous velocity approaches that of the freestream velocity. Consider the row of Fig. 8 at  $t/T = 0.375$ . When  $\sigma = 0.1$ , with a negative, normalized lift, the wake has discernable, alternating shed vortices from both the upper and lower surfaces with the airfoil at approximately zero angle of attack. In contrast,  $\sigma = 0.4$ , compared with the lower surge amplitude, has a turbulent wake structure with a compressed wake height due to increased momentum. The  $\sigma = 0.7$  case has these same characteristics, but even more pronounced than that of the middle amplitude of  $\sigma = 0.4$ .

At the negative, surge motion peak,  $t/T = 0.750$  and  $\sigma = 0.1$ , the wake has regained a periodic vortical structure and fully turbulent boundary layer. The  $\sigma = 0.4$  case has a less coherent vortical wake and trailing edge separation that moved from the trailing edge toward the leading edge along the upper surface as time progressed. The separation progression at  $t/T = 0.750$  occurred at approximately the three-quarter chord. The  $\sigma = 0.7$  case boundary layer has begun to stagnate on the upper surface where the dye has coalesced and begun to form a leading-edge vortex (LEV). The significant loss of

momentum causes a considerable lift deficiency that is not captured by the theory.

At  $t/T = 1.00$ , the airfoil is at rest in the surge axis with respect to the freestream velocity for all three cases, but the surge accelerations are different magnitudes. Turbulent boundary-layer separation is still occurring at this time step for all three cases, and progresses toward earlier reattachment with respect to time as the surge amplitude increases. The earlier, normalized time of boundary-layer attachment combined with the increased acceleration and dynamic pressure lends to the differences of the advancing and retreating phase observations described above as surge magnitude increases.

### B. Theoretical and Experimental Equivalence

The lift-based equivalence that is investigated here is the construction of the primary in phase lift components due to surge–pitch–plunge. The amplitudes of each case are listed in Table 1, where the lift amplitudes of pitch and plunge are equivalent to cancel the secondary harmonics that arise due to surge coupling. The surge amplitude is then swept from 0.1 to 0.7, to investigate a range that corresponds from near zero up to the robust zone found in the analytical approach.

At the low surge amplitude of 0.1, reduced frequency of 0.1, and high pitch amplitude of  $8.0^\circ$  the unsteady effects are most readily observed. Figure 10 corresponds to a part of the advancing phase of the experimental  $\sigma = 0.1$  case for Figs. 11a and 11b. The times selected in Fig. 10 represent key differences between theory and experiment in the normalized lift as it is affected by the viscous separation behavior of the boundary layer.

Note that  $t/T = 0.117$  when the separation of the turbulent boundary layer began to translate along the upper surface from the trailing edge toward the leading edge. This is a relatively small change in the rise of the lift, but it begins the advancing phase boundary-layer effects. This type of separation continued until approximately three-quarter chord, when local boundary-layer thickness minima occurred at the midchord at  $t/T = 0.186$ . The minima continued toward the leading edge along the upper surface and partitions the previous separation zone from an LEV formation reaching to the midchord. The leading-edge to midchord boundary LEV continued to form from  $t/T = 0.248$  to  $t/T = 0.270$ , and temporarily stopped the lift from decreasing. By  $t/T$  of 0.28, the LEV has absorbed the midchord to trailing edge zone and has fully separated. At this time the lift has momentarily stabilized and is termed “lift plateau,” where the quasi-steady normalized lift in Fig. 11b reveals that the lift is almost behaving as if it were steady, with a value just above one. The lift plateau ended at  $t/T = 0.28$  as the LEV shed. The Kelvin–Helmholtz shear layer instability that is seen at  $t/T = 0.28$  formed and dissipated as the airfoil continued to reduce in lift magnitude and plunged down and away from the separation.

The boundary layer for the reduced frequency of 0.10 remained separated until a reattachment time of  $t/T = 0.655$  occurring while the airfoil surged away from the flow and plunged upward. This is

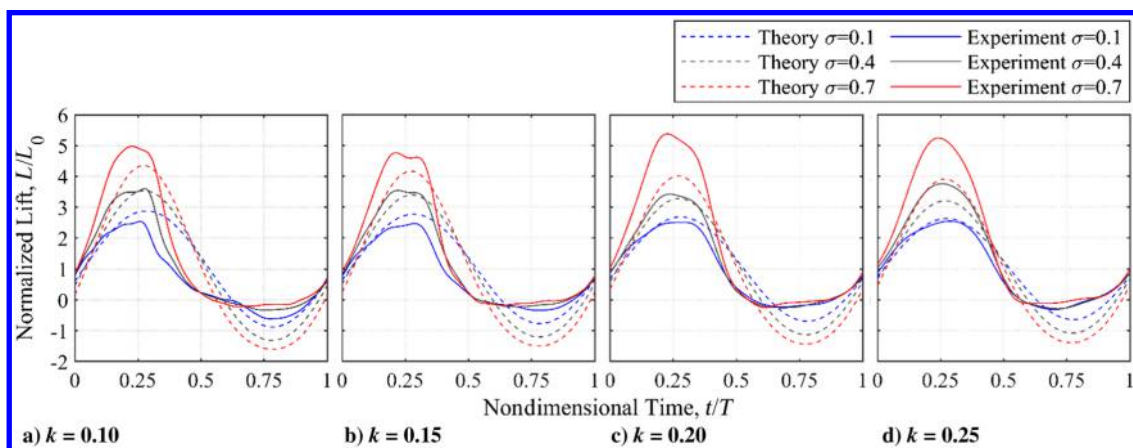


Fig. 7 Case C, G, K, and O lift equivalence over reduced frequency range 0.10–0.25 for  $\theta_m = 6.0^\circ$  for surge amplitudes 0.1, 0.4, and 0.7.

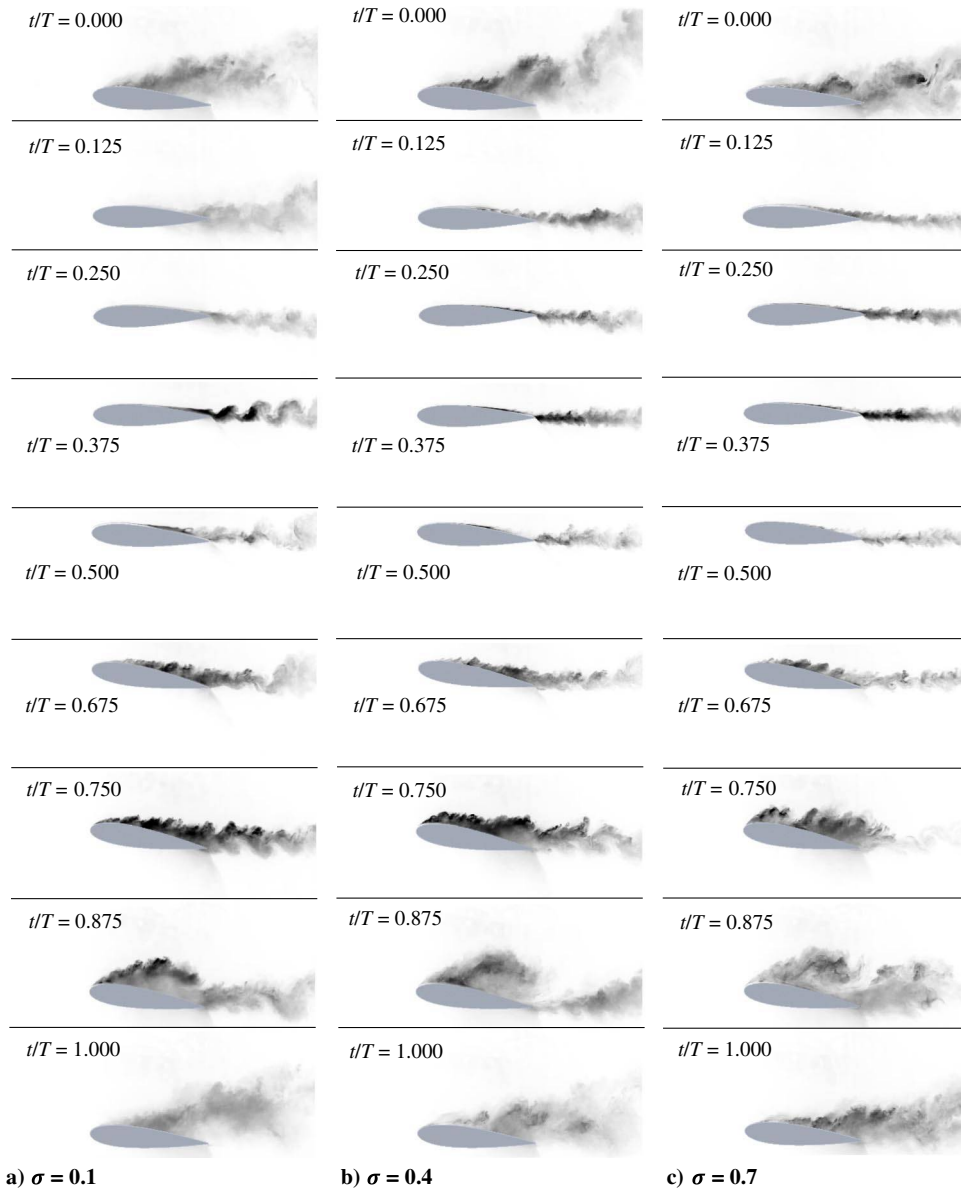


Fig. 8 Dye visualization for case G lift cancellation on the effects of surge amplitude of  $\sigma = 0.1, 0.4, \text{ and } 0.7$ .

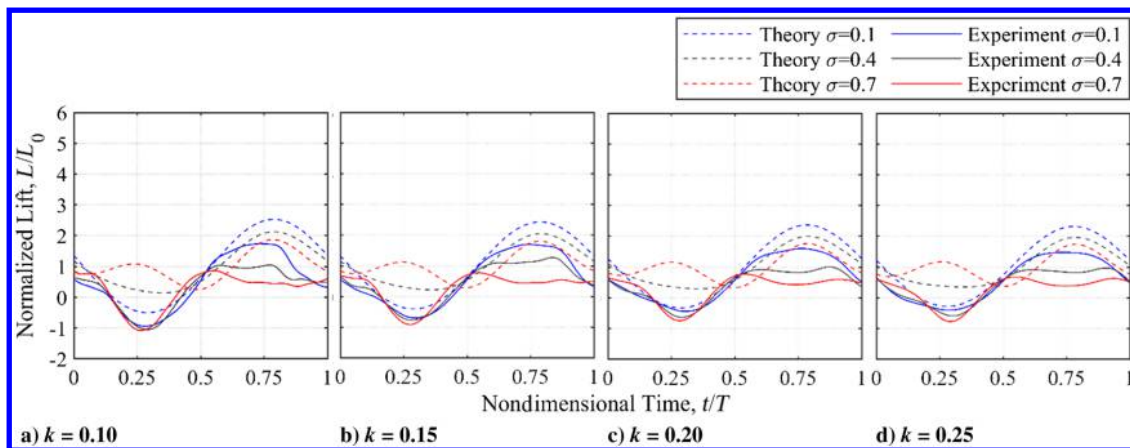
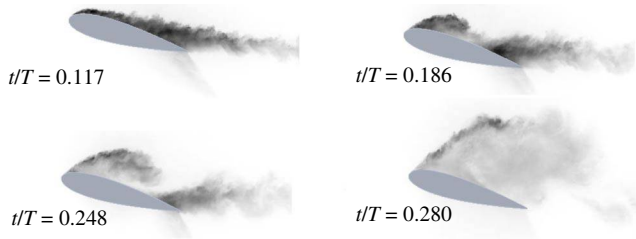


Fig. 9 Case C, G, K, and O lift cancellation over reduced frequency range 0.10–0.25 for  $\theta_m = -6.0^\circ$  for surge amplitudes 0.1, 0.4, and 0.7.

also when renewed trailing edge separation began. At lower surge amplitude this marked a change from separated lift behavior to that of attached flow that is similar to the theoretical prediction through the rest of the retreating phase. This is seen in Fig. 11a from this time until

the end of the cycle. This similarity continues to break down as the surge amplitude increases. In contrast, as the surge amplitude reaches 0.7 the boundary layer does not reattach until the advancing phase of the cycle is reached again.



**Fig. 10** Short time lapse of case D dye visualization for lift equivalence for  $\sigma = 0$ .

It is shown in comparison of Figs. 11–12 that the separation effects at lower reduced frequency have significantly more influence on the lift behavior than at higher reduced frequencies. A large difference is that the peak lift no longer truncates before the peak motion velocity is reached as occurred in Fig. 11.

The normalized lift scale in Fig. 12 has been kept the same as Fig. 11 for direct comparison. The corresponding dye visualization for Fig. 12 has similar boundary-layer structures that occur as the reduced frequency has increased from 0.10 to 0.25, but do not cause the same effect on normalized lift behavior. From reduced frequency of 0.10 to 0.25 the LEV formation does not occur until a change in  $t/T$  of 0.05 later. This is not a large time change, and it is thought that the change in normalized lift behavior is due to the increasing dominance of noncirculatory effects and dynamic pressure.

The other distinct difference with the increase in reduced frequency is that reattachment in the retreating phase does not occur

until much later. This is after  $t/T$  of 0.75 for the surge amplitudes equal to and below 0.4.

As the surge amplitude increases to 0.7 the boundary layer does not reattach with trailing edge separation until  $t/T = 0.115$ . Just before this time the separation location began at approximately three-quarter chord and continued to move toward the trailing edge until the new cycle's midchord local boundary-layer thickness minima occurred (similar to Fig. 10,  $t/T = 0.186$ ). The separation location then moved along the upper surface toward the leading edge until the separated LEV dissipated, just before a shear layer formed and dispersed. As the airfoil plunged upward, another weak LEV formed and advected along the upper surface, causing the small retreating phase peak in lift for surge amplitude of 0.7. This LEV does not occur at the lower surge amplitudes due to some amount of leading-edge reattachment occurring in the retreating phase.

### C. Theoretical and Experimental Cancellation

The differences between theory and experiment for cancellation are less pronounced than for the respective equivalence cases of the same parameters, with the exact negative pitch and plunge amplitudes. The cancellation motion is considerably different from a more typical motion like the previous equivalence motions discussed. The negative lift peak amplitudes of pitch and plunge are placed in phase by the angle  $\Psi$ ; and then in phase with the maximum surge lift peak by the angle,  $\phi$  demonstrated in Fig. 3b.

Maximum lift now occurs in the retreating phase instead of the advancing phase (with the exception of surge amplitude of 0.7 and pitch amplitudes of  $3^\circ$ , as shown in Fig. 13). The retreating phase also contains the significant vortex roll-up and shedding (if it is present for

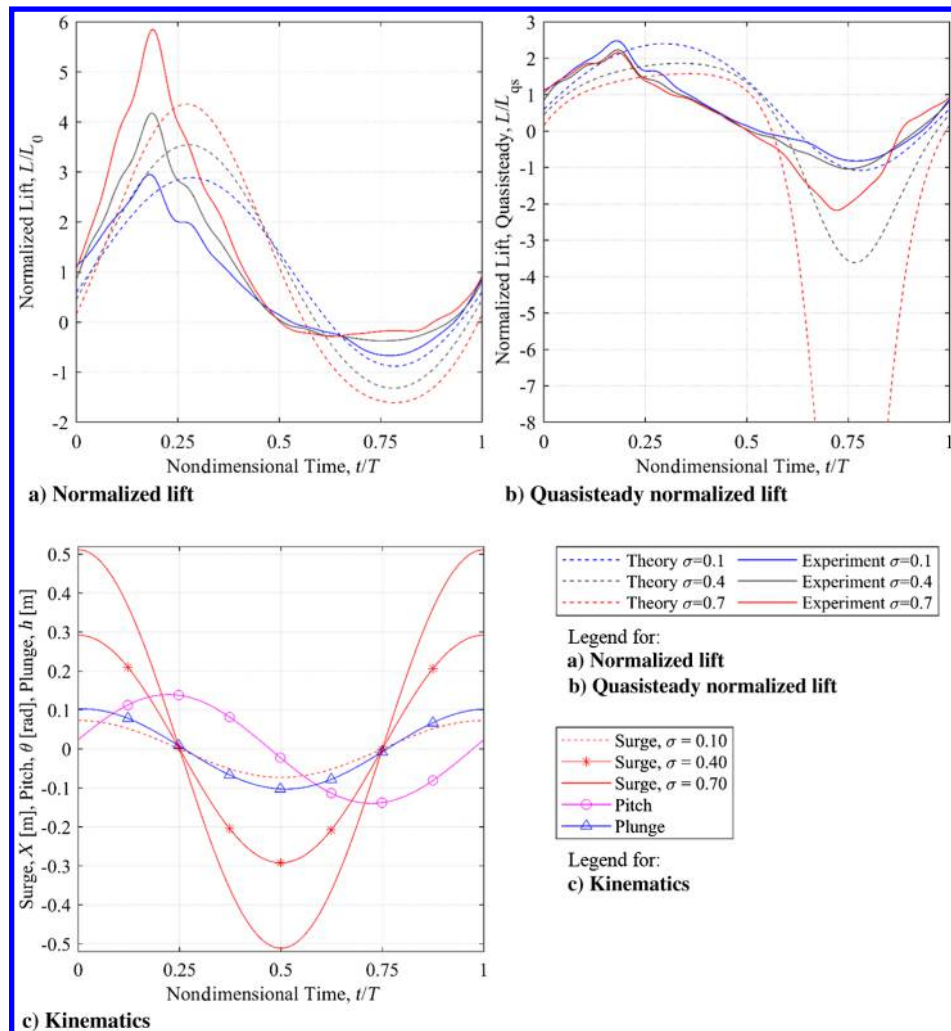


**Fig. 11** Case D lift equivalence and kinematics for theory and experimental normalized lift for surge amplitudes  $\sigma = 0.1, 0.4, \text{ and } 0.7$ .

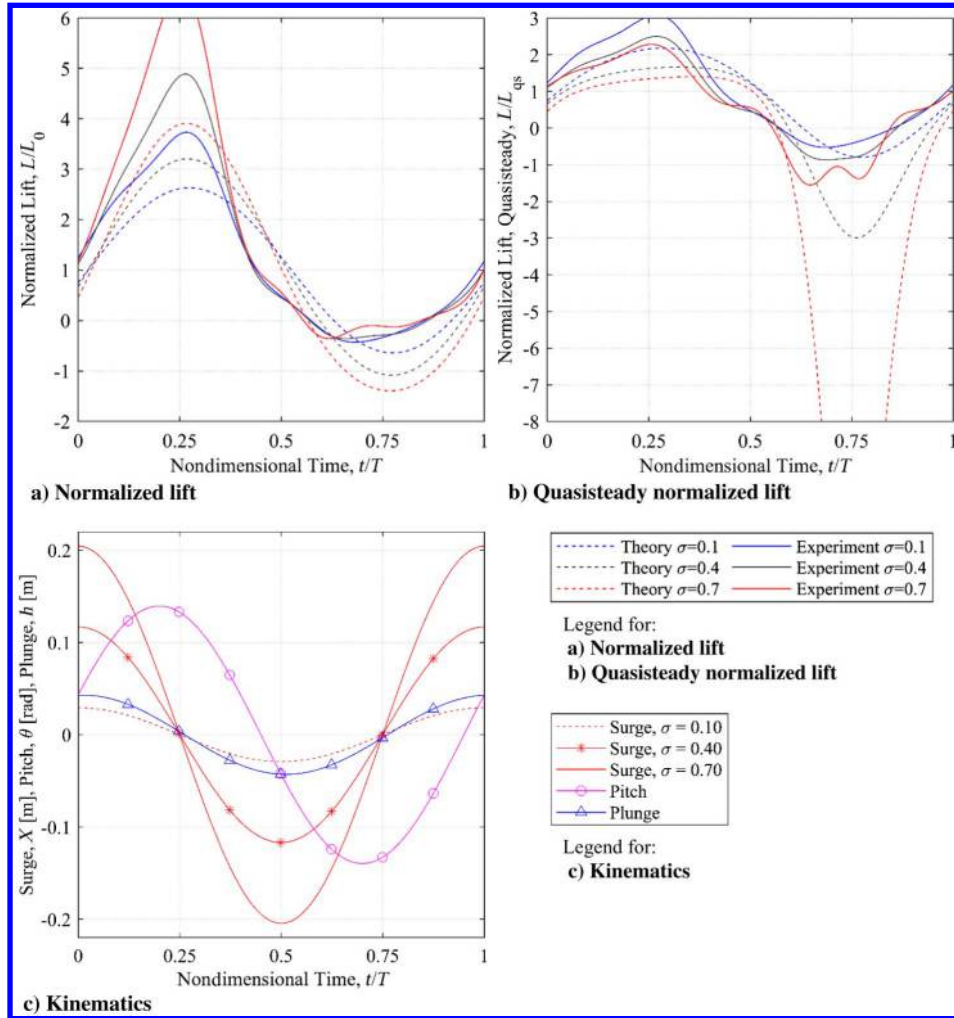


Fig. 12 Case P normalized lift equivalence and kinematics for theory and experimental normalized lift for surge amplitudes,  $\sigma = 0.1, 0.4, \text{ and } 0.7$ .  $k = 0.25, \theta_m = 8.0^\circ, h_m = 0.294c, \Psi = 76.16^\circ, \phi = 86.2^\circ$ .

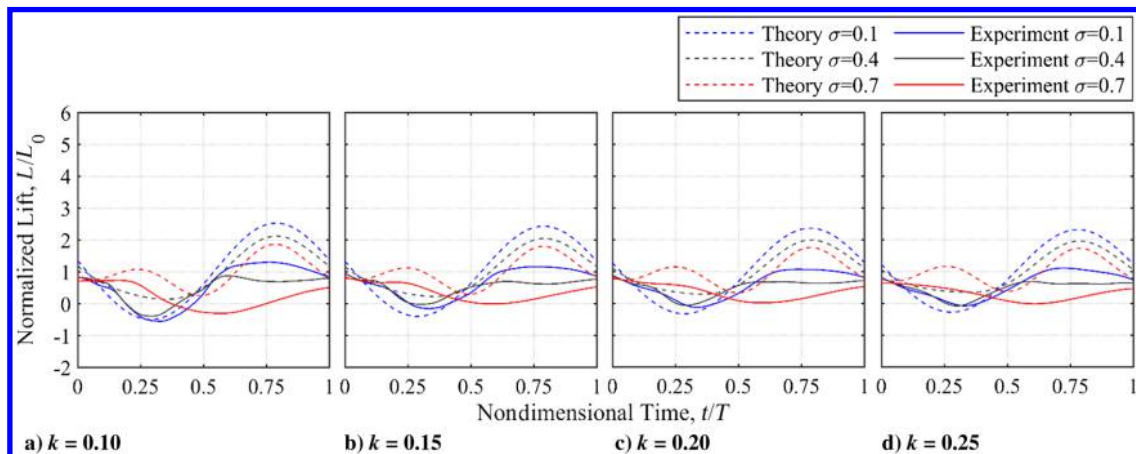


Fig. 13 Case A, E, I, and M lift cancellation theory and experiment for the reduced frequency range of 0.10–0.25 for  $\theta_m = -3.0^\circ$  for surge amplitudes 0.1, 0.4, and 0.7.

the parameter case). Despite never reaching a negative angle of attack, the advancing phase suction side of the airfoil appears to switch to the lower surface based on lift force measurements. This is due to plunging upward and pitching down as the airfoil surges forward. The experimental negative lift peaks increased as the surge amplitude increased for the  $6^\circ$  and  $8^\circ$  pitch amplitude groups, and not the lower  $3^\circ$  group. This is shown when comparing Figs. 9 and 13,

corresponding to the  $3^\circ$  and  $6^\circ$  groups, respectively. This is the opposite trend from what the theoretical analysis predicts for the  $6^\circ$  and  $8^\circ$  groups. This lends itself to the theory analysis of the advancing phase for cancellation having an agreeable, predicted trend the more the boundary layer remains attached.

Figure 14 is a dye visualization cycle that corresponds to the normalized cancellation lift plot of Fig. 13d. At  $t/T$  of 0.000 the

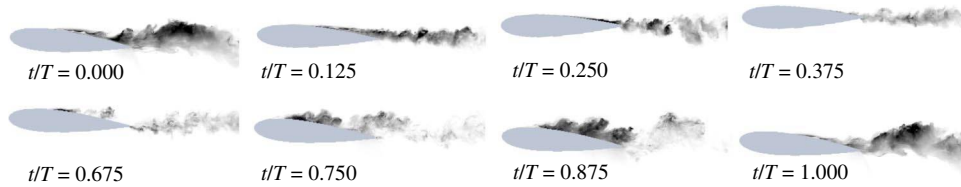


Fig. 14 One cycle time lapse of dye visualization for case M lift cancellation for  $\sigma = 0.7, k = 0.25, \theta_m = -3.0^\circ, h_m = -0.135c, \Psi = 76.16^\circ, \phi = 86.2^\circ$ .

airfoil has increased relative surge velocity back to freestream magnitude from the proceeding cycle's retreating phase. The airfoil begins to pitch down, plunge up, and surge forward. As the increase in surge velocity slows and reverses direction at  $t/T$  of 0.25, the boundary layer and wake thin until the retreating phase is reached. As the surge velocity slows, the boundary-layer thickness expands as the airfoil moves through  $t/T$  of 0.75. At  $t/T$  of 0.75 the relative surge velocity of the airfoil is only 30% of the freestream velocity. The loss in momentum does not advect the boundary layer downstream sufficiently quicker than the airfoil retreating surge motion.

However, the change in momentum is not large enough to cause the wake to be in front of the leading edge, indicating no reverse flow. By  $t/T$  of 0.875 the airfoil has almost regained enough momentum to advect the thicker boundary layer into the wake as the cycle is completed.

This cycle of dynamic pressure stretches and compresses the boundary-layer thickness and causes normalized lift magnitude differences between theory and experiment. The trend of increased lift in the advancing phase as surge amplitude increases is intact while the boundary layer does not have any large-scale separations.



Fig. 15 First half of the retreating phase time lapse of dye visualization for case P lift cancellation of  $\sigma = 0.7, k = 0.25, \theta_m = -8.0^\circ, h_m = -0.294c, \Psi = 76.16^\circ, \phi = 86.72^\circ$ .

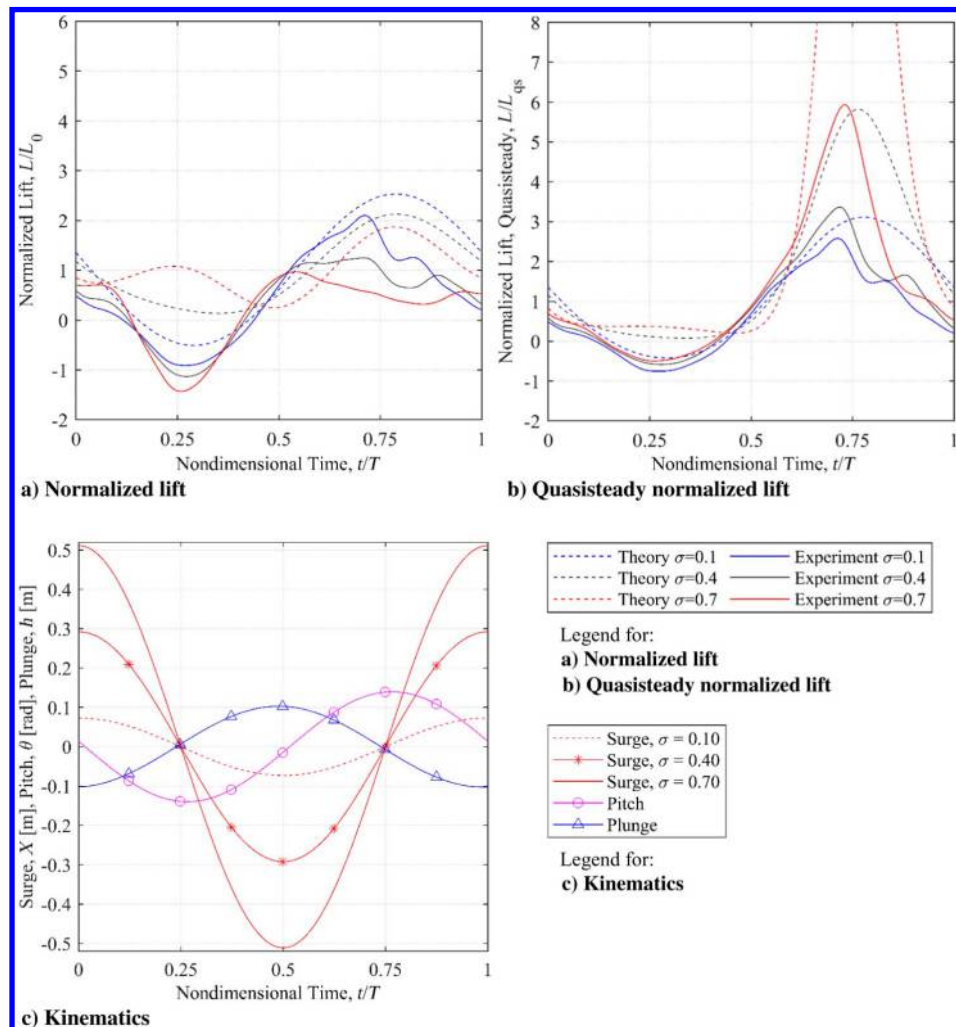


Fig. 16 Case D normalized lift cancellation and kinematics for theory and experimental normalized lift for surge amplitudes  $\sigma = 0.1, 0.4, \text{ and } 0.7. k = 0.10, \theta_m = -8.0^\circ, h_m = -0.704c, \Psi = 84.28^\circ, \phi = 85.75^\circ$ .

As the boundary-layer behavior changes with increased pitch and plunge amplitudes, so too does the effect on the normalized lift. Figure 15 shows dye visualization for the first half of a retreating phase where large separation occurs. Just as the surge retreating phase at  $t/T$  of 0.500 begins, the trailing edge separation ends, and the boundary-layer separation location moves along the upper surface toward the leading edge. This causes a weak vortex roll-up to occur at approximately three-quarter chord. The thin boundary layer just upstream of this vortex appears to cause a pressure difference sufficient enough to form a stronger midchord vortex formation as the airfoil continues to slow down with respect to the freestream, plunge down, and pitch up.

These motions and presence of downstream vortices continue to help sustain the existing vortex core and promote a new LEV formation. By  $t/T$  of 0.675 the weak three-quarter chord vortex has nearly dissipated while the airfoil experiences a local lift minima. The LEV continues to become larger while the midchord vortex weakens and becomes less coherent. By  $t/T$  of 0.750 the midchord vortex has almost completely advected downstream along the upper surface. The LEV separates and advects downstream as a shear layer instability, lasting approximately  $t/T$  of 0.05, occurs through the end of the cycle and the boundary layer reattaches with trailing edge separation at  $t/T$  of 0.110.

Cancellation lift plateaus occur in the retreating phase with lower reduced frequencies and separated flows. Similar normalized lift plateau behavior occurred in the advancing phase of the equivalence cases. Despite the similar effect on normalized lift behavior, the boundary-layer separation location along the upper surface from trailing edge to leading edge can be very different between the cancellation and equivalence cases. This is demonstrated by the midchord separation vortex that only appeared in cancellation cases, Fig. 15 being an example case.

Figure 16b demonstrates that the halt in lift decline representing the plateau requires a quasi-steady normalized lift just above one. As the surge amplitude increases, the normalized lift plateau becomes a concave, local minima until  $\sigma$  of 0.6. Although the normalized lift behaviors for surge amplitudes of 0.1 and 0.4 are quite different, the unsteady behaviors in the quasi-steady plot are approximately the same magnitude of 1.5. The quasi-steady normalized lift in Fig. 11b for the equivalence cases is also approximately the same magnitude of 1.5 when the normalized lift plateaus occur. This is consistent throughout the parameter study, where the trend is that as the reduced frequency increases, the quasi-steady normalized lift falls below the magnitude of 1 and does not cause lift plateaus.

## VI. Conclusions

The closed-form Greenberg theory of unsteady lift for surge–pitch–plunge oscillations remains attractive due to being a linearized predictive method for a nonlinear problem. The theory is often applied to two-dimensional aerodynamics that are well outside of the constraints of flat plate potential flow (which assumes fully attached flow, flat plate chord line boundaries, a trailing edge Kutta condition, and planar wake). Further simplifications are implemented in the Greenberg theory to achieve a closed-form solution. The assumptions of uniform velocity perturbation along the chord line and the use of high frequency in the wake integrals to achieve oscillatory wake forms were made, which effectively limits the theory to small surge amplitude approximations.

Here, two types of surge–pitch–plunge oscillatory motion are considered: equivalence and cancellation. The lift components for cancellation were chosen to build on the pitch–plunge Theodorsen solution by McGowan. With pitch and plunge having equivalent magnitude, the surge amplitude that would cause the most cancellation was determined. This was done analytically by first introducing a phase angle  $\phi$  between the two translating motions of surge and plunge while excluding pitch. With the average, time-dependent surge–plunge phase angle determined, the pitch components were reconsidered in a reduced Greenberg theory that only includes the primary lift and secondary coupled terms.  $\phi$  is a commutative phase bridge between surge–plunge and pitch–plunge to equate the phase

shift between surge and pitch, represented by  $\Psi + \phi$ . With both phase angles defined, a closed-form theory for cancellation between surge–pitch–plunge was derived.

The Greenberg theory predictions for lift-based equivalence and cancellation were more agreeable to flow conditions that were closer to attached flow with trailing edge separation at lower amplitude rates. As the reduced frequency increased to 0.25, the circulatory effects became less dominant as noncirculatory effects increased. It was observed that the theory overpredicts the phase shift in lift that occurs due to an increase in reduced frequency.

Despite the violation of the Kutta condition and massively separated LEVs, the theory did hold some agreement to experimental lift. The differences in momentum for lift-based equivalence and cancellation create unsteady flow structure similarities between the two motion types' advancing and retreating phase motions. With increasing surge amplitude, the advancing phase momentum gain amplifies the influence of these flow structures on the experimental, normalized lift, whereas the momentum loss in the retreating phase reduces this influence. Based on these observations, even when the low inertial Reynolds number of 40,000 is considered, the closed-form Greenberg theoretical analysis presented in this work is a suitable first-step approximation method for airfoil lift behavior in the case of sinusoidal combinations of surge–pitch–plunge lift-based equivalence and cancellation.

## Acknowledgments

This work was supported by the North Carolina Coastal Sciences Institute. The authors are grateful to Craig Cox for help with the hardware–software integration of the planar motion mechanism.

## References

- [1] Maresca, C., Favier, D., and Rebont, J., "Experiments on an Aerofoil at High Angle of Incidence in Longitudinal Oscillations," *Journal of Fluid Mechanics*, Vol. 92, No. 4, 1979, pp. 671–690. <https://doi.org/10.1017/S0022112079000823>
- [2] Granlund, K., Monnier, B., Ol, M. V., and Williams, D., "Airfoil Longitudinal Gust Response in Separated vs. Attached Flows," *Physics of Fluids*, Vol. 26, No. 2, 2014, Paper 027103. <https://doi.org/10.1063/1.4864338>
- [3] Greenblatt, D., Mueller-Vahl, H., Strangfeld, C., Medina, A., Ol, M. V., and Granlund, K. O., "High Advance-Ratio Airfoil Streamwise Oscillations: Wind Tunnel vs. Water Tunnel," AIAA Paper 2016-1356, 2016. <https://doi.org/10.2514/1.J056408>
- [4] McGowan, G. Z., Granlund, K., Ol, M. V., Gopalarathnam, A., and Edwards, J. R., "Investigations of Lift-Based Pitch–Plunge Equivalence for Airfoils at Low Reynolds Numbers," *AIAA Journal*, Vol. 49, No. 7, 2011, pp. 1511–1524. <https://doi.org/10.2514/1.J050924>
- [5] Baik, Y. S., Bernal, L. P., Granlund, K., and Ol, M. V., "Unsteady Force Generation and Vortex Dynamics of Pitching and Plunging Airfoils," *Journal of Fluid Mechanics*, Vol. 709, Oct. 2012, pp. 37–68. <https://doi.org/10.1017/jfm.2012.318>
- [6] Ol, M., "Vortical Structures in High Frequency Pitch and Plunge at Low Reynolds Number," *37th AIAA Fluid Dynamics Conference and Exhibit*, AIAA Paper 2007-4233, June 2007.
- [7] Rival, D., and Tropea, C., "Characteristics of Pitching and Plunging Airfoils Under Dynamic-Stall Conditions," *Journal of Aircraft*, Vol. 47, No. 1, 2010, pp. 80–86. <https://doi.org/10.2514/1.42528>
- [8] Sunada, S., Kawachi, K., Matsumoto, A., and Sakaguchi, A., "Unsteady Forces on a Two-Dimensional Wing in Plunging and Pitching Motions," *AIAA Journal*, Vol. 39, No. 7, 2001, pp. 1230–1239. <https://doi.org/10.2514/2.1458>
- [9] Strangfeld, C., Rumsey, C., Müller-Vahl, H., Greenblatt, D., Nayeri, C., and Paschereit, C., "Unsteady Thick Airfoil Aerodynamics: Experiments, Computation, and Theory," *45th AIAA Fluid Dynamics Conference, AIAA Aviation Forum*, AIAA Paper 2015-3071, 2015. <https://doi.org/10.2514/1.J056408>
- [10] Favier, D., Agnes, A., Barbi, C., and Maresca, C., "Combined Translation/Pitch Motion: A New Airfoil Dynamic Stall Simulation," *Journal of Aircraft*, Vol. 25, No. 9, 1988, pp. 805–814. <https://doi.org/10.2514/3.45663>
- [11] Dunne, R., Schmid, P. J., and McKeon, B. J., "Analysis of Flow Timescales on a Periodically Pitching/Surging Airfoil," *AIAA Journal*,

- Vol. 54, No. 11, 2016, pp. 3421–3433.  
<https://doi.org/10.2514/1.J054784>
- [12] Choi, J., Colonius, T., and Williams, D., “Surging and Plunging Oscillations of an Airfoil at Low Reynolds Number,” *Journal Fluid Mechanics*, Vol. 763, Jan. 2015, pp. 237–253.  
<https://doi.org/10.1017/jfm.2014.674>
- [13] Leung, J. M., Wong, J. G., Weymouth, G. D., and Rival, D. E., “Modeling Transverse Gusts Using Pitching, Plunging, and Surging Airfoil Motions,” *AIAA Journal*, Vol. 56, No. 8, 2018, pp. 3271–3278.  
<https://doi.org/10.2514/1.J056961>
- [14] Greenberg, J. M., “Airfoil in Sinusoidal Motion in a Pulsating Stream,” NACA TN 1326, 1947.
- [15] Theodorsen, T., “General Theory of Aerodynamic Instability and the Mechanism of Flutter,” NACA TR 496, 1935.
- [16] Wagner, H., “Über die Entstehung des dynamischen Auftriebs von Tragflügeln,” *Zeitschrift für angewandte Mathematik und Mechanik*, Bd. 5, Heft 1, Feb. 1925, pp. 17–35.
- [17] Isaacs, R., “Airfoil Theory for Flows of Variable Velocity,” *Journal of the Aeronautical Sciences*, Vol. 12, No. 1, 1945, pp. 113–117.  
<https://doi.org/10.2514/8.11202>
- [18] Van der Wall, B. G., and Leishman, J. G., “On the Influence of Time-Varying Flow Velocity on Unsteady Aerodynamics,” *Journal of the American Helicopter Society*, Vol. 39, No. 4, Oct. 1994, pp. 25–36.  
<https://doi.org/10.4050/JAHS.39.25>
- [19] Greenblatt, D., “Unsteady Low-Speed Wind Tunnels,” *AIAA Journal*, Vol. 54, No. 6, 2016, pp. 1817–1830.  
<https://doi.org/10.2514/1.J054590>
- [20] Stewart, E., “Design, Analysis, and Validation of a Free Surface Water Tunnel,” M.Sc. Thesis, North Carolina State Univ., Raleigh, NC, Sept. 2017.
- [21] Mueller, T. J., “Low Reynolds Number Aerodynamics,” *Proceedings of the Conference*, Springer Science & Business Media, Notre Dame, IN, Vol. 54, 1989, pp. 281–292.
- [22] Visbal, M. R., “Numerical Investigation of Deep Dynamic Stall of a Plunging Airfoil,” *AIAA Journal*, Vol. 49, No. 10, 2011, pp. 2152–2170.  
<https://doi.org/10.2514/1.J050892>

H. Dong  
 Associate Editor